



Self-curling electroconductive nerve dressing for enhancing peripheral nerve regeneration in diabetic rats

Can Liu^{a,c,d,e,1}, Lei Fan^{b,f,1}, Zhenming Tian^{a,d,e,1}, Huiquan Wen^g, Lei Zhou^b, Pengfei Guan^{a,d,e}, Yian Luo^h, Chuncheung Chan^{a,d,e}, Guoxin Tan^h, Chengyun Ning^{b,***}, Limin Rong^{a,d,e,**}, Bin Liu^{a,d,e,*}

^a Department of Spine Surgery, The Third Affiliated Hospital of Sun Yat-sen University, Guangzhou, 510630, China

^b College of Materials Science and Technology, South China University of Technology, Guangzhou, 510641, China

^c Department of Orthopedic Surgery, The First Affiliated Hospital of Zhejiang University, Hangzhou, 310003, China

^d Guangdong Provincial Center for Quality Control of Minimally Invasive Spine Surgery, Guangzhou, 510630, China

^e Guangdong Provincial Center for Engineering and Technology Research of Minimally Invasive Spine Surgery, Guangzhou, 510630, China

^f Department of Orthopedic Surgery, Nanfang Hospital, Southern Medical University, Guangzhou, 510515, China

^g Department of Radiology, The Third Affiliated Hospital of Sun Yat-Sen University, Guangzhou, 510630, China

^h School of Chemical Engineering and Light Industry, Guangdong University of Technology, Guangzhou, 510006, China

ARTICLE INFO

Keywords:

Diabetic peripheral nerve injury
Electroconductive hydrogel
Axonal regeneration
Nerve remyelination

ABSTRACT

Conductive scaffolds have been shown to exert a therapeutic effect on patients suffering from peripheral nerve injuries (PNIs). However, conventional conductive conduits are made of rigid structures and have limited applications for impaired diabetic patients due to their mechanical mismatch with neural tissues and poor plasticity. We propose the development of biocompatible electroconductive hydrogels (ECHs) that are identical to a surgical dressing in this study. Based on excellent adhesive and self-healing properties, the thin film-like dressing can be easily attached to the injured nerve fibers, automatically warps a tubular structure without requiring any invasive techniques. The ECH offers an intimate and stable electrical bridge coupling with the electrogenic nerve tissues. The *in vitro* experiments indicated that the ECH promoted the migration and adhesion of the Schwann cells. Furthermore, the ECH facilitated axonal regeneration and remyelination *in vitro* and *in vivo* through the MEK/ERK pathway, thus preventing muscle denervation atrophy while retaining functional recovery. The results of this study are likely to facilitate the development of non-invasive treatment techniques for PNIs in diabetic patients utilizing electroconductive hydrogels.

1. Introduction

Peripheral nerve injury (PNI) is a common clinical disease in patients suffering from diabetes mellitus (DM), which could lead to permanent deficits in locomotor functions and sensory perception [1]. It has been demonstrated that diabetic patients suffering from these impairments are more susceptible to deficits in axon regeneration after PNI [2,3]. This is because long-term hyperglycemia and insulin resistance aggravate nerve dysfunction, leading to segmental axon demyelination and

slow regrowth of injured nerves, in addition to neuromuscular atrophy [4]. The distal portion of the peripheral nerve gets disconnected after the injury and undergoes Wallerian degeneration (WD), which involves a catastrophic breakdown of the neural cytoskeleton into cellular debris [5,6]. Although the intrinsic regeneration capacity of the nerve has been confirmed, it is insufficient to ensure a complete functional recovery.

Electrically conductive scaffolds have shown potential in enhancing nerve viability and neuronal differentiation [7,8]. Previous studies have shown that improving the electrostatic cell-cell and cell-scaffold

Peer review under responsibility of KeAi Communications Co., Ltd.

* Corresponding author. Department of Spine Surgery, The Third Affiliated Hospital of Sun Yat-sen University, Guangzhou, 510630, China.

** Corresponding author. Department of Spine Surgery, The Third Affiliated Hospital of Sun Yat-sen University, Guangzhou, 510630, China.

*** Corresponding author.

E-mail addresses: imcnying@scut.edu.cn (C. Ning), ronglm@mail.sysu.edu.cn (L. Rong), liubin6@mail.sysu.edu.cn (B. Liu).

¹ The first three authors contributed equally to this work and should be considered as co-first authors.

<https://doi.org/10.1016/j.bioactmat.2021.03.034>

Received 4 February 2021; Received in revised form 19 March 2021; Accepted 20 March 2021

2452-199X/© 2021 The Authors. Publishing services by Elsevier B.V. on behalf of KeAi Communications Co. Ltd. This is an open access article under the CC

BY-NC-ND license (<http://creativecommons.org/licenses/by-nc-nd/4.0/>).

interactions can significantly improve the possibility of nerve regrowth and remyelination, thereby resulting in complete overall recovery [9, 10]. Existing conductive electroactive materials, such as polypyrrole (PPy), polyaniline (PAni), and polythiophene (PTh), have gained popularity and are used to design artificial nerve conduits [11,12]. However, these conventional conduits have rigid structures and are incompatible with neural tissues, in addition to being inadhesive and non-elastic [9,13]. These properties of conventional conduits generally require further trimming of the residual nerve fibers to suture the conduit to the distal end [14]. A surgical intervention involving sutures or insertion of conduits to bridge the gaps is unsuccessful against diabetic nerve injuries. This is because the regeneration of injured nerves is extremely slow (~1 mm/day) and exclusively accompanied by severe demyelination due to the complex neurophysiological defects of patients suffering from DM [15]. In addition, invasive interventions and the insertion of mismatched implants can result in additional trauma and complications, such as scarring, increased inflammation, and progressive WD [16,17]. Therefore, the biomaterials used for the treatment of diabetic nerve crush injuries should be soft, adhesive, biocompatible, and capable of insertion through a non-invasive procedure.

Three-dimensional (3D) polymer hydrogel dressings, characterized by their adhesive properties and biomimetic microenvironments that are similar to those of native soft tissues, are widely used for wound healing, corneal defects, stomach ulcers, and burn injuries [18]. Recent breakthroughs in the development of hydrogel dressings have made them permeable to soluble factors and impermeable to bacteria [18,19]. This creates a local environment that is moist, elastic, and capable of resisting deformation. These soft and self-healing hydrogel dressings can be easily adjusted to form a secure wrapping intimately around nerve fibers and match the shape of any damaged nerve tissue without adopting invasive methods due to their tissue-mimicking mechanical properties [20,21]. It can also serve as a protective barrier for the surrounding tissues, thereby reducing adverse immune responses, preventing fibrous tissue ingrowth and nerve scarring, and providing a favorable environment for nerve regeneration [16,22]. These favorable properties of the hydrogel dressing have simplified the cumbersome installation process and made it a promising candidate for the treatment of nerve-crushed injuries in DM patients. However, the lack of conductive electroactivity and bioactive factors limits its therapeutic applications in PNI.

Biocompatible electroconductive hydrogel (ECH) dressings that have excellent mechanical properties and electroactivity have been developed in this study to achieve localized neuromodulation. The biocompatible ECH dressing, which consists of tannic acid (TA) and PPy, is soft, water-rich, adhesive, and self-healing. As a highly conductive thin film attached to the injured nerve in diabetic models and automatically wrapped in a size-matched tubular structure, it develops a stable and intimate electrical bridge coupling with the electrogenic nerve tissues to promote axon regeneration and remyelination. The micromorphological, electrical, and mechanical properties of the conductive hydrogels are validated in this study. The cell biocompatibility, adhesion, and migration of the Schwann cells (SCs), and axonal extension of nerve cells on the hydrogel were evaluated *in vitro*. Further, a diabetic sciatic nerve injury model was established to study the role of the ECH in promoting nerve regeneration and functional recovery.

2. Materials and methods

2.1. Synthesis of ECH hydrogel

The synthesis process involved the dissolution of tannic acid (TA, Aladdin, Shanghai, China) in deionized (DI) water to obtain TA solution. The hydrogels with two different TA compositions were prepared by varying TA concentration as follows: ECH-1, 0.15 wt%, and ECH-2, 0.6 wt%. The solution I was prepared by the addition of 0.5 mmol of pyrroles (py, 99%, Aldrich, St. Louis, USA) to 0.6 ml TA solution, followed by stirring. Solution II was prepared by dissolving 0.316 g ferric chloride

hexahydrate (FeCl₃·6H₂O, 98%, Aladdin, Shanghai, China) powder in 0.6 ml water (4 °C). Solutions I and II were gently mixed at 4 °C to promote gelation. The hydrogels were incubated in distilled water (DI) overnight at 4 °C to remove any remaining reaction reagents.

2.2. Characterization of hydrogels

2.2.1. Fourier transform infrared spectroscopy (FTIR)

The chemical composition and functional groups of the samples were detected by FTIR. The hydrogels were ground into a powder and treated with D₂O after lyophilization. The spectra were obtained in transmission modes over 32 scans at a 4 cm⁻¹ resolution using a Nicolet IS10 spectrometer (Thermo Scientific, USA).

2.2.2. Scanning electron microscopy (SEM)

The micromorphology and network of samples were examined at an accelerating voltage of 10 kV through SEM (Quanta 200, FEI, Netherlands). The hydrogels were dehydrated and sputter-coated with platinum (Pt) for 60 s, followed by scanning observation.

2.2.3. Rheological experiments

Rheological measurements of the samples were performed using a rotary rheometer (Physica MCR301, Anton Paar, Austria). The dynamic oscillation frequency (10–0.1 Hz) was conducted at a fixed strain (1%). The storage modulus (*G'*) and loss modulus (*G''*) were obtained from the typical linear regions of the frequency–modulus curves.

2.2.4. Electrical characterization

The conductive capability, which includes the cyclic voltammetry (CV) and electrochemical impedance (EIS), was evaluated using an electrochemical workstation (Zennium Zahner, Germany). A platinum mesh and Ag/AgCl were used as the counter and reference electrodes, respectively. Hydrogels were anchored on indium-tin oxide (ITO) glass and tested in a phosphate-buffered saline (PBS) electrolyte solution (pH = 7.4, 0.1 M). The CV measurements were performed at a sweep rate of 10 mV/s and ranged from –0.8 V to 1.0 V. The EIS spectra were evaluated at open circuit potentials that ranged from 100 kHz to 0.01 Hz.

2.3. *In vitro* studies

2.3.1. Rat dorsal root ganglion (DRG) isolation and cell cultures

The dorsal root ganglions (DRG) were obtained from day 2 postnatal Sprague–Dawley (SD) rats using an established method [23]. The DRGs were dissected with forceps, and the membranes around them were peeled off. The ganglia were then planted on the ECH-1, ECH-2, and standard glass in the DRG culture medium (Neurobasal-A (Gibco) supplemented with 2% B-27 (Gibco), 1 × glutamine (Gibco), 50 ng/mL nerve growth factor (NGF, PeproTech), and 1 × penicillin/streptomycin (Gibco)). The medium was replaced every 3 days. The RSC-96 and PC-12 cells were purchased from ATCC (Manassas, USA). These cells were cultured in Dulbecco's modified Eagle's medium (DMEM, Gibco) that contained 10% fetal bovine serum (FBS, Gibco) and were maintained in a humid atmosphere (37 °C, 5% CO₂).

2.3.2. Cell viability and biocompatibility measurement

The viability of the RSCs was detected using a live/dead cytotoxicity kit (calcein-AM/PI, Invitrogen) and cell counting kit-8 solution (CCK-8, Dojindo, Japan), as specified by the manufacturer. RSCs were planted on the different samples and double-stained with calcein-AM and propidium iodide for 15 min at room temperature. CCK8 solution (1:10) was added to each group on the first, third, and seventh days. The optical density (OD) was calculated using an enzyme-labeling instrument (Multiskan FC, Thermo) at a wavelength of 450 nm. The cell viability was calculated by comparing the percentage of OD in the hydrogels and control groups. Blood samples were collected and co-incubated with ECH for 4 h, followed by centrifugation at 12,000g for 5 min at 4 °C. PBS

and Triton-100X were used as blank and positive group, respectively. The absorbance was measured, and the haemolysis percentage was calculated using the following Equation:

$$\text{Hemolysis}(\%) = \frac{\text{Sample absorbance} - \text{Negative control}}{\text{Positive absorbance} - \text{Negative control}} \times 100\%$$

2.3.3. Cell adhesion and migration evaluation

The RSCs were seeded on the slides that were covered with ECH-1 and ECH-2, and standard glass was used as control. Cell adhesion and spreading were detected by cytoskeleton staining through green actin tracking after 3 days of culture. For migration assay, a longitudinal scratch was made on each slide to create an artificial wound when the cells attained a confluence of 80–90%. The samples were washed twice with PBS to remove the detached cells and then stained with calcein-AM (Invitrogen, USA) after culture for 12 and 24 h. The images were captured using a laser confocal reflection microscope (Leica, Germany).

2.3.4. Immunofluorescence (IF)

The cells or tissues were placed in a 4% paraformaldehyde solution for 30 min. Following that, they were permeabilized and blocked with 3% BSA and 0.1% Triton-X for 1 h at room temperature. The samples were incubated with their corresponding primary antibodies at 4 °C overnight, followed by the secondary antibodies for 1 h. The antibodies used in this study are listed in Table 2. Hoechst 33,342 (Sigma) was used to stain the nucleus. The stained micrographs were visualized with a laser confocal reflection microscope (Leica, Germany).

2.3.5. Gene expression

The total RNA was extracted by using the mRNA extraction kit (Omega) and then reverse transcribed into cDNA using the PrimeScript™ RT reagent kit (TaKaRa). The qRT-PCR analysis was performed by using the LightCycler 480 SYBR Green Master Mix (TaKaRa). The primers used in this study are provided in Table 2. The gene expression was calculated using the 2-ΔΔCt method.

2.3.6. Western blot (WB)

The samples were washed with PBS and lysed with a RIPA protein extraction reagent (CWBI, China) that contained protease and phosphatase inhibitors (Thermo Fisher, USA). The suspensions were then centrifuged, and the supernatant was retained and preserved. The total protein concentration was determined using a BCA assay (Thermo Fisher, USA). Equal amounts (40 μg) of protein were subjected to SDS-PAGE electrophoresis and passed through polyvinylidene fluoride membranes (PVDF, Millipore, USA). The membranes were probed with the corresponding primary antibodies (Table 1) at 4 °C overnight and

Table 1
Primary and secondary antibodies.

Antibodies	Species	Type	Dilution (IF/WB)	Source
Anti-Neurofilament (NF)	Rabbit	Polyclonal IgG	1:400/ 1:1000	CST, America
Anti-Myelin basic protein (MBP)	Mouse	Monoclonal IgG	1:400/ 1:1000	Abcam, England
Anti-S100 beta (S100)	Rabbit	Monoclonal IgG	1:400/ 1:1000	Abcam, England
Anti-Growth-associated protein-43 (GAP43)	Rabbit	Polyclonal IgG	1:1000	Genetex, America
Anti-MEK1/2	Mouse	Monoclonal IgG	1:1000	CST, America
Anti-Phospho-MEK1/2 (Ser217/221)	Rabbit	Monoclonal IgG	1:1000	CST, America
Anti-p44/42 MAPK (Erk1/2)	Rabbit	Monoclonal IgG	1:1000	CST, America
Anti-Phospho-MAPK (Erk1/2) (Thr202/Tyr204)	Rabbit	Monoclonal IgG	1:1000	CST, America

Table 2
PCR primers.

Primer Name	Forward	Reverse
NF	GGAGTGGTTCGAGTGAGATTG	CCTTGGTGCTTTTCAGTGCCT
GAP43	GCACATCGGCTTGTAGGCT	GGAGGGAGATGGCTCTGCTACT
TUJ1	CCCGTTTTAGCCACCTTTGTATT	CCCTCCAAATATAAACACAACCC
SYN	CTTCTGGTTGGGGACTACTCTC	GCGAACACGGCTGTAGCCAGAAAG
GAPDH	AGACAGCCGCATCTTCTGT	CTTGCCGTGGGTAGATGCAT

then bathed with the secondary antibodies. A protein density analysis was performed using Tanon 5200 (Tanon Science & Technology, China).

2.4. In vivo studies

2.4.1. Ethics statement

All experimental procedures involving animals were approved by the Animal Experimentation Ethics Committee of Sun Yat-sen University and performed following the Guidelines for the Care and Use of Laboratory Animals, as specified by the Ministry of Public Health and National Institutes of Health.

2.4.2. Animals and surgical procedures

Adult female SD rats (220–240 g) were purchased from the Guangdong Medical Laboratory Animal Center (Guangzhou, China). A total of 40 animals were randomly divided into two groups, namely the control group (n = 10) and the diabetes group (n = 30). The diabetic SD rats received intraperitoneal injections of streptozotocin (STZ) buffer at a dose of 70 mg/kg, while the control group was treated with an equal volume of PBS. According to established guidelines, a casual blood glucose concentration greater than 16.7 mmol/L indicated the presence of DM [24]. The rats that did not meet the blood glucose requirements were considered to have failed in the diabetes model and were excluded from the study before the commencement of the experimental procedure. The blood glucose values of the control and STZ-diabetic rats were 5.37 ± 1.53 mmol/L and 34.15 ± 3.98 mmol/L, respectively, as shown in Table 3.

The diabetic rats were anesthetized by an intraperitoneal injection of a mixture of xylazine (10 mg/kg) and ketamine (70 mg/kg). Three experimental groups were included in the study, namely the sham-diabetes (n = 8), PNI (n = 8), and electroconductive hydrogel treatment (ECH, n = 8) groups. The crushed injuries of sciatic nerves models in the diabetes group were performed according to the procedure previously described [25,26]. The sciatic nerve was exposed using a gluteal muscle blunt dissection method. A crushed injury model was induced at a location 5 mm proximal to the sciatic notch using two vascular clips (Oscar, China) with 30 g force for 2 min. The ECH-2 was placed around the defective area of the sciatic nerve, while its ends were overlapped to form a tubular structure (Fig. 4A). The sham group underwent identical surgical procedures for anesthesia, skin and muscle operations then closed, while the PNI group's crushed sciatic nerve surgery was performed without hydrogel implantation. Following the experimental procedures, the animals were kept warm and well-fed under standard conditions.

Table 3
Body weight and blood glucose for control (Con) and diabetic rats (DM).

	Con	DM
Initial weight (g)	225.2 ± 6.7	226.3 ± 3.9
Final weight (g)	257.6 ± 7.6	182.3 ± 10.0
Initial glucose (mmol/dL)	4.85 ± 1.06	4.98 ± 0.83
Final glucose (mmol/dL)	5.37 ± 1.53	34.15 ± 3.98

2.4.3. Functional analysis

The walking track analysis was conducted to assess motor function recovery 14, 21, and 28 days after the operation. The rats were trained to walk across a narrow walkway with their hind paws covered in black ink (non-toxic). Five measurable footprints were recorded to calculate the sciatic function index (SFI), including PL (distance from the heel to the third toe), TS (distance from the first to the fifth toe), and IT (distance from the second to the fourth toe). A schematic diagram depicting the measured footprint parameters is shown in Fig. 4C. E and N represent the experimental and normal groups, respectively. The SFI was calculated using the following formula:

$$\text{SFI} = -38.3 \times (\text{EPL} - \text{NPL})/\text{NPL} + 109.5 \times (\text{ETS} - \text{NTS})/\text{NTS} + 13.3 \times (\text{EIT} - \text{NIT})/\text{NIT} - 8.8.$$

2.4.4. Electrophysiological assessment

Electrophysiological assessments were conducted to evaluate the functional recovery 28 days after the operation using an established method [27]. The animals were anesthetized, and the injured sciatic nerves were re-exposed. Bipolar electrodes were attached at the proximal end of the regenerated nerves to generate electrical signals. Further, an electrode was inserted into the belly of the ipsilateral gastrocnemius muscle to generate the electromyograph (Fig. 4F). The compound muscle action potentials (CMAPs) of the injured nerve were

compared with those on the contralateral side to perform a comparative analysis.

2.4.5. Histological assessment of muscle and nerve fibers

Regenerated nerves and gastrocnemius muscles were placed in a 4% paraformaldehyde solution for 24 h before being embedded in paraffin. Longitudinal paraffin nerve sections of 10 μm were stained through hematoxylin-eosin (H&E) staining to evaluate nerve morphology. The morphological changes in the 30 μm cross-sections of the ipsilateral gastrocnemius muscle were examined through H&E and Masson trichrome staining (MTS). The representative images of each sample were obtained by using a light microscope.

2.4.6. Transmission electron microscopy (TEM) and morphological analyses

The central portions of the regenerated nerves were removed 4 weeks after surgery. The tissues were post-fixed, embedded in epoxy resin, and cut into 50 nm ultrathin cross-sections and 1 μm semi-thin cross-sections. The ultrathin sections were used for TEM (JEOL, Tokyo, Japan), while the semi-thin sections were stained with toluidine blue staining (TBS). Five images of the samples were randomly selected to evaluate the morphology of the myelinated axons.

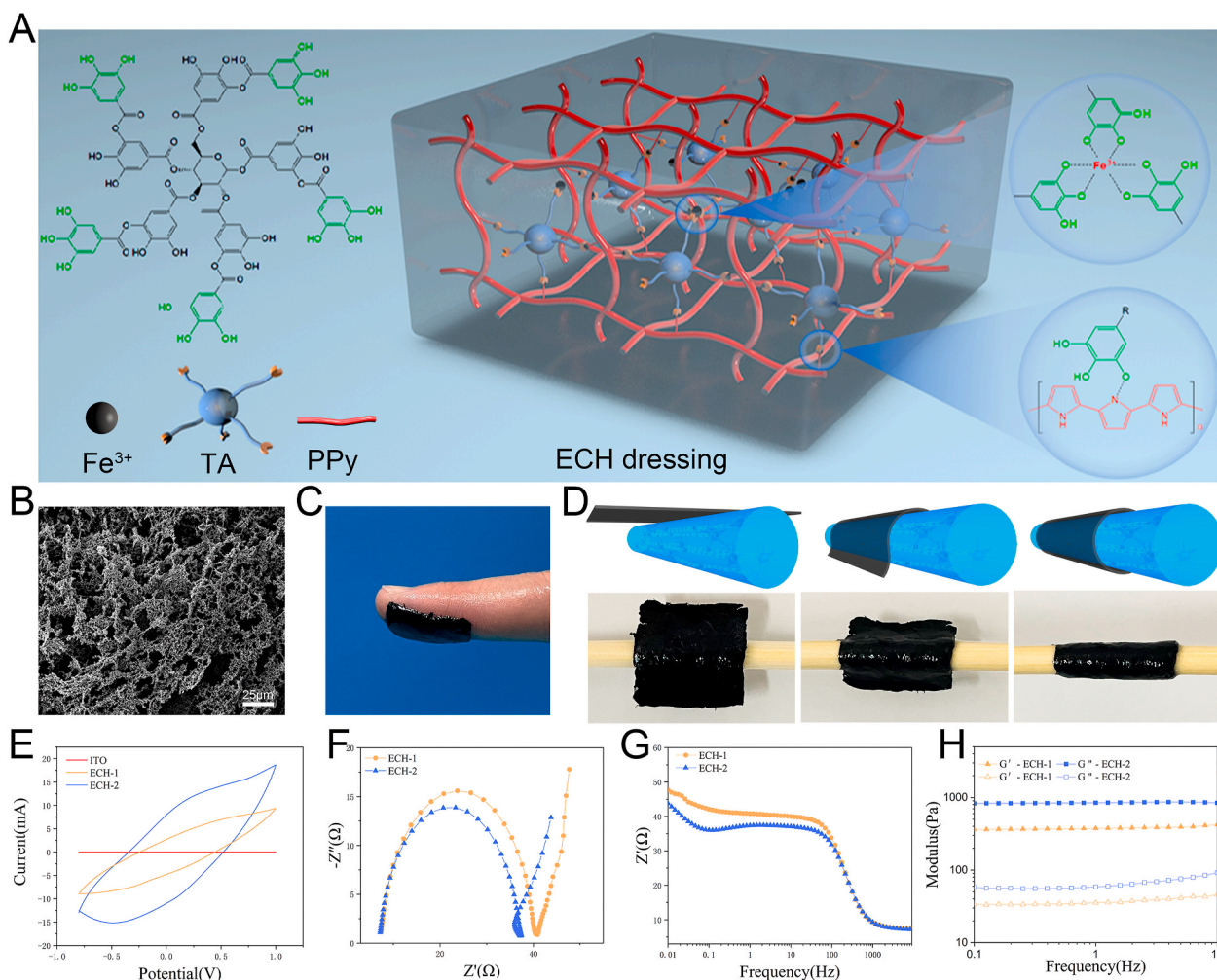


Fig. 1. Characterization of ECHs. (A) Schematic of ECH formation and chemical structure. TA crosslinks with PPy chains by intermolecular electrostatic interactions and Fe^{3+} acts as an oxidant and ionic crosslinker. (B) SEM image of the ECH. (C) A photograph of a dressing film plastered on the finger showed the adhesive properties of the ECH. (D) Illustrations and photographs showed self-curling ECH warped a size-matched tubular structure. (E–G) Electrical characterization, including (E) cyclic voltammograms, (F) Nyquist curves, and (G) Bode plots of ECH hydrogels showed excellent electrical performance. (H) The mechanistic properties of ECHs.

2.5. Statistics

Quantitative data were expressed as mean \pm standard deviation (SD). The results were statistically analyzed according to one-way ANOVA, followed by Dunn's or Tukey's multiple comparisons test. The statistical analysis was carried out using the Service Solutions (SPSS, version 22.0, Chicago, USA) and GraphPad Prism software (GraphPad Software, version 5, San Diego, USA). The p-value was set at < 0.05 as the level of significance.

3. Results and discussion

3.1. Fabrication of ECH

The chemical structure and functional groups of the ECH are presented in Fig. 1A. The hydrogel was formed by instant gelation (within 2s) due to the crosslinking of TA and PPy in the presence of an oxidative initiator (FeCl_3). Intermolecular electrostatic interactions occur between the phenol hydroxy groups of TA and the protonated nitrogen groups of PPy. Further, TA acts as a dopant and protonates the nitrogen atom of PPy to become conductive. The Fe^{3+} ions play a significant role in the gelation process by acting as the oxidant and ionic crosslinkers. Excessive Fe^{3+} ions promote the polymerization of Py through oxidation and also form ionically crosslinked networks with TA.

3.2. Characteristics of ECH

The FTIR spectrum of the ECH is consistent with that of pristine polypyrrole (PPy), thereby indicating that PPy is the main component of the synthesized hydrogel. The stretching vibrations of the $\text{C}-\text{N}^+$ bonds and $\text{C}=\text{N}^+-\text{C}$ bonds in the ECH spectrum are located at 1174 cm^{-1} and 903 cm^{-1} , respectively, thereby indicating that the conductive hydrogel is in a highly doped state [28] (Fig. S1). The ECH displayed multiple 3D layers and highly aligned porous microstructures in the SEM evaluation (Fig. 1B). Interconnected globular nanoparticles were observed on the surface of the hydrogels, which facilitated the instantaneous interfacial interaction among the nanomaterial and the cells and tissues (Fig. S2) [29]. This promotes cell adhesion and effective substance exchange, including nutrients and waste.

Moreover, the ECH can be easily plastered onto irregular objects, such as fingers and nerve tissue (Fig. 1C). The tissue adhering nature enables the ECH to automatically adhere to any object to warp a size-matched tubular structure. (Fig. 1D). This allows the ECH to simplify the cumbersome installation process of traditional scaffolds in vivo applications, especially in diabetics: scaffolds need to let fragile injured nerves pass through them, and need to be sutured with residual nerve fibers for fixation [22,30]. The porous surface and hydrophilic properties of the ECH facilitate adhesion with the native nerve tissue. After self-adhering, the ends of the hydrogel contact with each other and quickly reintegrate as a monolithic wrap structure through a self-healing process, which attributed to the reversibility of the dopant and coordination bonds. Following the self-curling phenomena, the ECHs attained the form of a size-matched wrap structure and maintained its excellent apposition with the injured nerve tissue (Fig. Video1).

The electronic properties of different hydrogels were evaluated by carrying out CV and EIS measurements. The ITO bare electrode displayed a negligible conductive response. Compared to the ITO electrode, the ECH-1 and ECH-2 showed significantly improved anodic and cathodic currents. The CV curves showed greater oxidation and reduction current values in ECH-2 than that of the ECH-1 hydrogel. This is attributed to the appropriate doping level and crosslinking density (Fig. 1E). It is accepted that the electrical conductivity increases with increasing doping levels and crosslinking density. In the Nyquist plots, a quasi-semicircle appeared in the high-frequency region for ECH-1 and ECH-2. The largest diameter of the semicircle was observed in the ECH-2 group, which exhibited good redox activity and high charge-transfer

resistance (Fig. 1F). In the Bode plot, the charge transfer resistance (RCT) decreases as the diameter of the semicircle decreases. As shown in Fig. 1G, the RCT of ECH-2 hydrogel was relatively low, indicating ECH-2 displayed better charge transfer characteristics than the ECH-1 hydrogel. Further, the Bode plot showed that the impedance values of the ECH-2 were very low between 300 Hz and 1 kHz (Fig. 1G), which is usually the most active communication frequencies between nerve cells [31]. This is beneficial for fast neural cell communication through endogenous bioelectric signals that are generated by the activity of ion channels and pumps between adjacent cells [32,33].

The mechanical properties of the extracellular matrix environment are the key factors affecting cell viability and function [34]. The storage modulus (elastic modulus G') is greater than the loss modulus (viscoelastic modulus G'') of the samples in the angular frequency range of 0.1–10 Hz, indicating that the hydrogel has excellent stability and viscoelasticity. The ECH-1 and ECH-2 hydrogels had average storage moduli of $846 \pm 12\text{ Pa}$ and $375 \pm 15\text{ Pa}$ during the dynamic mechanical analysis, respectively (Fig. 1H). This satisfies the requirements of the CNS tissue (100–1000 Pa), thus providing ideal flexibility and mechanical support for axon extension [35].

3.3. Schwann cell adhesion and migration on the ECHs

SCs are the principal glia of the peripheral nervous system. They provide metabolic support to the regenerated axons and affect the myelination process and the formation of nodal domains [36]. Cell viability, adhesion, and wound healing measurements were performed to evaluate the myelination capacity of SC. A significant number of viable cells (green) were observed on the hydrogels, as shown in Fig. 2A. The cell viability values of the cells cultured on different substrates exceeded 80% at each instant, thereby indicating that ECHs were non-cytotoxic and had excellent biocompatibility (Fig. 2B). The cytoskeleton images demonstrated that the spreading area and length of the SCs cultured on the ECH-2 hydrogel were significantly greater than those of the other groups, thereby indicating the presence of a good stretching state and strong interconnectivity (Fig. 2C). A significant amount of SCs in the ECH group spread out of the edges during the wound healing measurements and distributed themselves into the denuded area after 24 h (Fig. 2D). It is noteworthy that the SCs were more likely to cluster at the injury site in the ECH-2 group, whereas were distributed in a random and disorganized manner in the control group. The gap area of the ECH-2 group ($31.1 \pm 5.7\%$) was significantly lower than that of the ECH-1 ($45.5 \pm 2.6\%$) and control groups ($60.8 \pm 5.9\%$) (Fig. 2E). These results indicated that the electroconductive and hydrophilic properties of the ECH scaffolds made them suitable for cell attachment and migration.

3.4. Axonal outgrowth due to ECHs

The support provided for nerve regeneration was comparing by planting PC-12 and DRG cells on ECHs and standard glass (control). Neurofilaments (NF) and growth-associated protein-43 (GAP43), the specific markers of neurons and axons, were used to assess the capacity of hydrogels in neurite outgrowth. The PC-12 cells that were cultured on the ECH-2 hydrogel for 3 days displayed better activity and a greater average nerve length than those of other groups (Fig. 3A). The WB analysis confirmed that the concentrations of the NF and GAP43 post-synaptic markers in the ECH-2 group were higher than those in the ECH-1 and control groups (Fig. 3B and C).

The NF and GAP43 expression values in the ECH-2 group were approximately 5.2 times and 2.6 times greater than those observed in the control group (Fig. 3D). Besides, the gene expressions of TUJ1 and SYN, which represented the growth of primary axons, were also increased in the ECH-2 group (Fig. 3E). These readings were consistent with our WB and immunocytochemistry results. We further studied the ability of the hydrogels to enhance the growth of neuronal neurites in

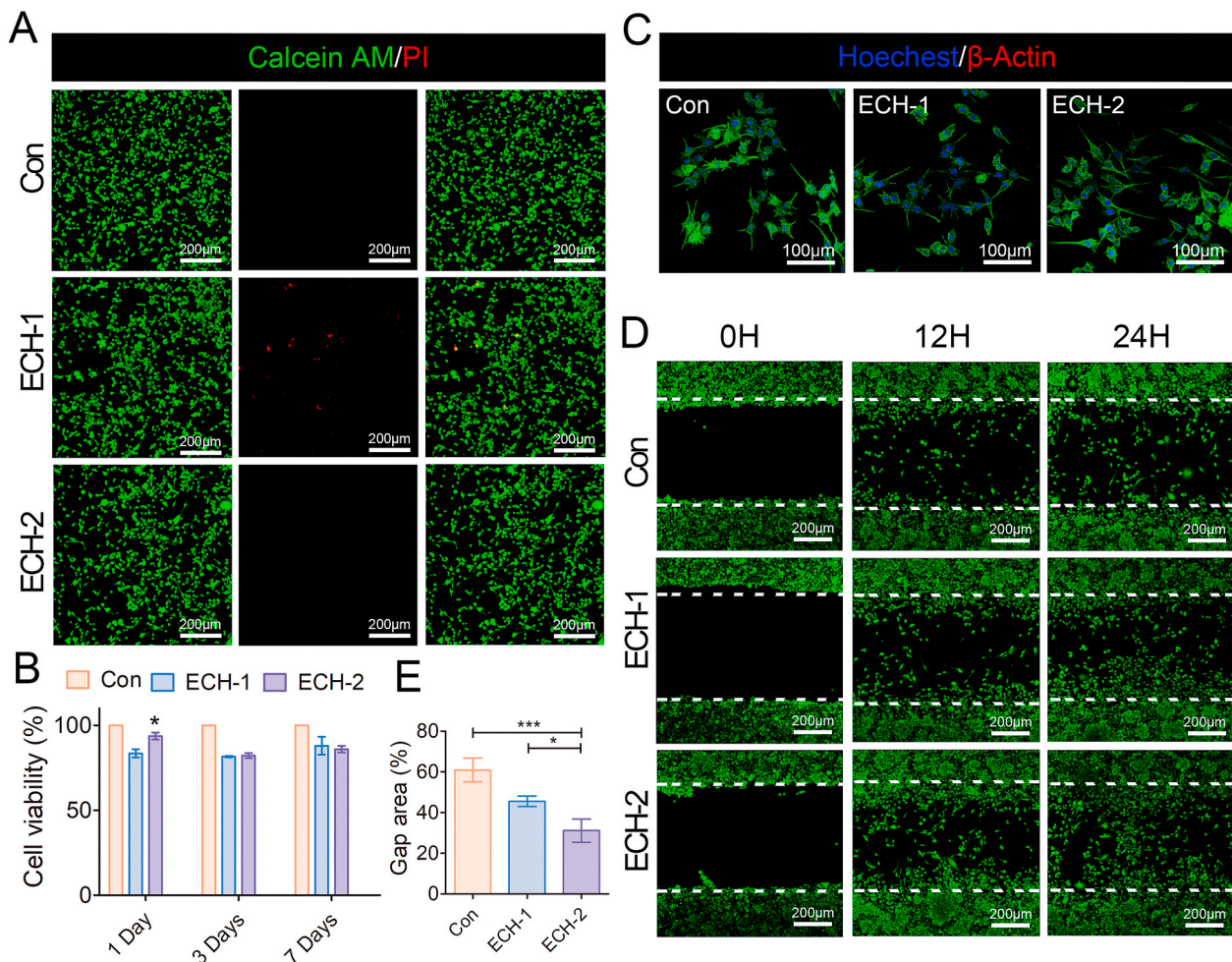


Fig. 2. In vitro Schwann cells adhesion and migration on ECHs. (A) Live/dead assay of the SCs cultured on the hydrogel for one day. The green and red staining represent the live and dead cells, respectively. (B) The CCK-8 assay indicated that the cell viability exceeded 80% for the hydrogels after seeding ($n = 5$). (C) Cytoskeleton images demonstrated the adhesion of SCs cultured on each sample. (D) Wound-healing migration assay of the SCs on the hydrogels and control slide. (E) Quantitative analysis of the gap area at the denuded site ($n = 3$). (* $p < 0.05$, ** $p < 0.01$, and *** $p < 0.001$). (For interpretation of the references to color in this figure legend, the reader is referred to the Web version of this article.)

the DRG in vitro. We observed extensive axonal sprouting from the DRG neurons in each group within the first day. It was observed on the third and seventh days that the DRG in the ECH-2 group was generating faster than it was in the ECH-1 and blank control groups, thereby indicating that the ECH-2 hydrogel was more effective in stimulating axonal regeneration in vitro (Fig. 3F) than the ECH-1 and control groups. Moreover, the density and length of DRG axons were quantified (Fig. 3G and H). The density of axons in the ECH-2 hydrogel group was significantly higher than those in the other groups. Besides, the axon length in the ECH-2 group was 1.64 ± 0.16 mm, which was significantly longer than that in the ECH-1 (0.95 ± 0.13 mm) and control group (0.45 ± 0.07 mm). Thus, it is evident that the density and length of axon spreading in the ECH-2 hydrogel were greater than those in the other groups. These observations indicated that the ECH-2 hydrogel has an excellent potential for nerve outgrowth, which can be attributed to its superior electrical activity.

3.5. Functional and morphological evaluation of regenerated nerves

To detect the ability of the ECH-2 to facilitate nerve repair, the thin film-like hydrogel dressing was easily attached to a 5 mm long crushed nerve, resulting in the automatic formation of a tubular structure (Fig. 4A). Hemocompatibility is an important in vivo indicator for evaluating the haemolytic activity of implanted materials. As shown in

Fig. S3A, serum extracted from ECH co-incubated whole blood showed light yellow color, similar to that of the PBS control group, but the Triton-100X group was bright red in color. The haemolysis ratios of ECH were 0.71% (Fig. S3B). Locomotor function recovery is related to the structure and pathophysiology of the sciatic nerve injury. A histological evaluation indicated that the axonal fibers in the ECH group were well organized at the injured site. However, the nerve fibers in the PNI group were sparse, disordered, and had a significant lesion volume (Fig. 4B). Thus, the hydrogel provided a suitable microenvironment for axonal regeneration.

The SFI is a reliable and widely used index to measure motor function recovery after PNI. It ranges from 0 (normal function) to -100 (complete dysfunction) and is calculated by measuring footprint parameters, such as the print length, intermediate toe spread, and toe spread [37] (Fig. 4C). A plateau was observed in the motor recovery after two weeks of hydrogel treatment and maintained until the end of the study. The animals in the ECH group (score = -38.3 ± 3.3) demonstrated a significantly greater improvement in motor function than their counterparts in the PNI group (score = -76.2 ± 2.0) four weeks after the operation (Fig. 4D). The footprints demonstrated an increment in the print lengths, and a reduction in the intermediate toe spreads and toe spreads after a serious injury that results in the loss of nerve and muscle function. The ECH treatment group demonstrated unambiguous gaits with the most superior toe spread, while the PNI group reported reduced

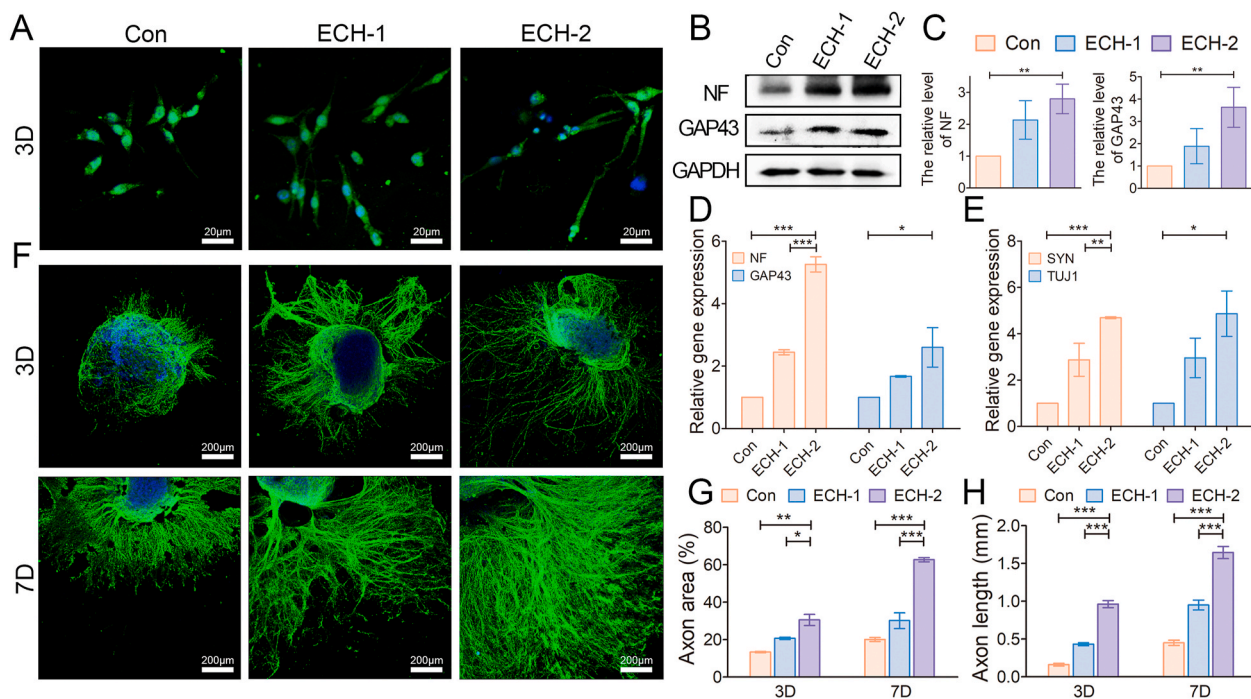


Fig. 3. Axonal outgrowth on the ECHs. (A) Immunocytochemistry of the PC-12 cells for the NF (green) and cell nuclei (blue) to analyze the axonal extension. (B) WB analysis to detect the NF and GAP43 expression values in PC-12 cells cultured in hydrogels and control conditions for 3 days. (C) Quantification of the integrated density for the protein bands (n = 3). (D–E) qRT-PCR data on the axonal gene expressions of the PC-12 cells. (F) Stained DRG for NF (green) and nuclei with DAPI (blue). (G–H) Analysis of the axonal lengths and distribution of the DRG for each group (n = 3). (*p < 0.05, **p < 0.01, and ***p < 0.001). (For interpretation of the references to color in this figure legend, the reader is referred to the Web version of this article.)

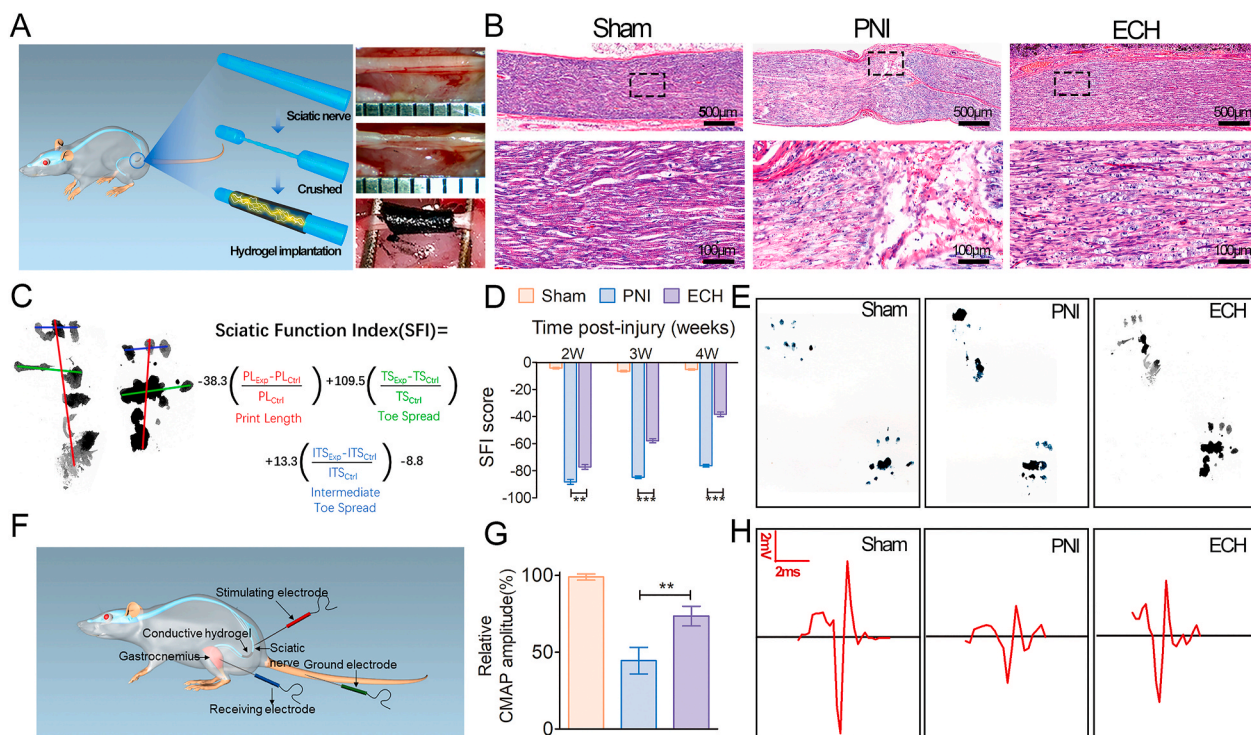


Fig. 4. Functional analysis and morphological evaluation of the regenerated nerves. (A) Hydrogel implantation in a diabetic rat with sciatic nerve defect. (B) Structural repair indicated by H&E staining of the sciatic nerve on the 28th day after the injury. (C) The equation for calculating the SFI and measurement parameters of the footprints. (D) SFI scores of different groups 14, 21, and 28 days after the operation (n = 5). (E) Representative analysis of the footprints. (F) Illustration of the CMAP testing protocol. (G) Quantification of the CMAP amplitudes measured in each group (n = 3). (H) Representative CMAP recordings on the injured side of the sciatic nerve (*p < 0.05, **p < 0.01, and ***p < 0.001).

toe spread and ankle movement impairment (Fig. 4E).

Electrophysiological measurements were used to assess nerve conduction and motor function recovery, which were indicated by the CMAP amplitude. The proximal end of the injured nerve was stimulated in each group, and the peak symmetry of CMAP was recorded, 4 weeks after the surgery (Fig. 4F). The ECH treatment group indicated peak symmetry, which was similar to that of the sham group and significantly higher than that of the PNI group (Fig. 4G and H). The enhanced CMAP amplitude is positively correlated with the density of the regenerative nerve fibers crossing the injured site and reinnervating the target muscles [38]. The findings indicated that the ECH was beneficial for the regeneration of fibers through the lesion, transmission of nerve impulses, and reactivation of target skeletal muscles.

3.6. Stimulation of axonal regeneration and remyelination through ECH treatment

The NF-200 protein, myelin basic protein (MBP), and S-100 β were evaluated by immunofluorescence staining on longitudinal nerve sections to evaluate axonal regeneration and remyelination four weeks after the injury. NF-200 represents regenerated neurofilaments and axons, and MBP is an important indicator of myelinated fibers. The ECH remained firmly attached to nerve tissue four weeks after transplantation (Fig. S4). No myelin-associated and consecutive long axons

were detected by NF-200 staining in the PNI group, as shown in Fig. 5A. However, NF-positive and MBP-positive cells were longitudinally distributed and well-oriented at the injury lesion in the ECH group, thereby confirming the existence of several regenerated myelinated nerve fibers that connected the two ends of the site. The WB evaluation was consistent with the IF results, thereby confirming that the NF and MBP protein expression values in the ECH group were higher than those in the PNI group at the injury site (Fig. 5B and C).

The SC-specific marker S-100 β is an indicator of the migration of SCs. The positive area percentages of S-100 β in the ECH group were higher than those in the PNI group. Further, they displayed a linear and orderly regenerating structure in the former, thereby confirming the formation of myelin sheaths that were composed of SCs (Fig. 6A). The WB analysis further proved that the expression of the S-100 β protein in the ECH group was significantly upregulated in comparison to that in the PNI groups (Fig. 6B and C). These observations revealed that the ECH hydrogel treatment significantly improved the remyelination of the nerve fibers. Endogenous bioelectrical signals are essential for neuron development and function. Intercellular interactions between the neurons and precursors through spontaneous electrical activity, even before the formation of synapses, affect regeneration events, such as neuronal differentiation, migration, myelination, and the establishment of neurotransmitter phenotypes [39,40]. The ECH acts as a conductive guidance bridge and facilitates a stable and intimate electrical coupling

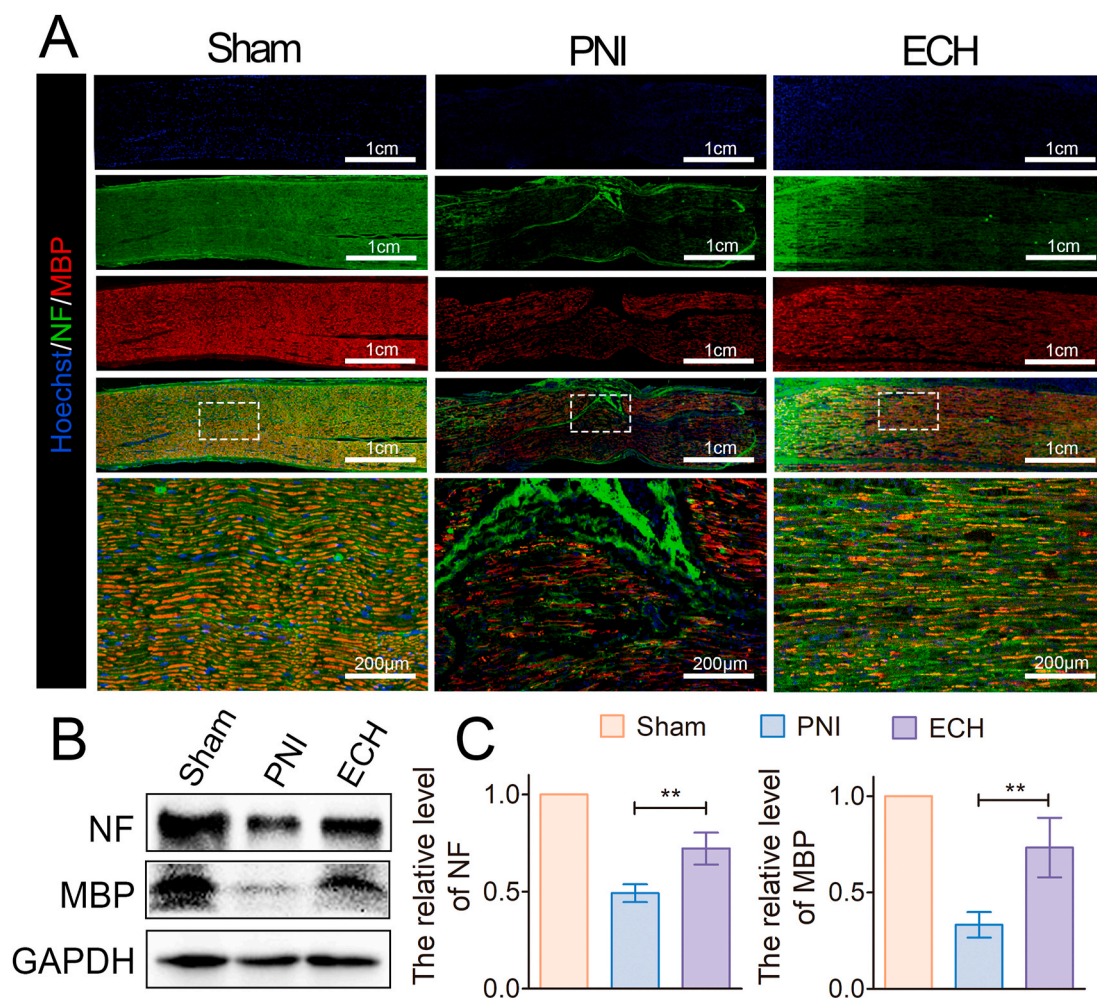


Fig. 5. Promotion of axonal regeneration by ECH treatment in diabetic PNI models. (A) Immunocytochemistry of the NF (green) and MBP (red) proteins in the sciatic nerve tissues on the 28th day after the injury. (B) WB analysis of the NF and MBP protein bands in the sham, PNI, and hydrogel groups. (C) Quantitative measurement of the protein band intensity of the NF and MBP proteins ($n = 3$) (* $p < 0.05$, ** $p < 0.01$, and *** $p < 0.001$). (For interpretation of the references to color in this figure legend, the reader is referred to the Web version of this article.)

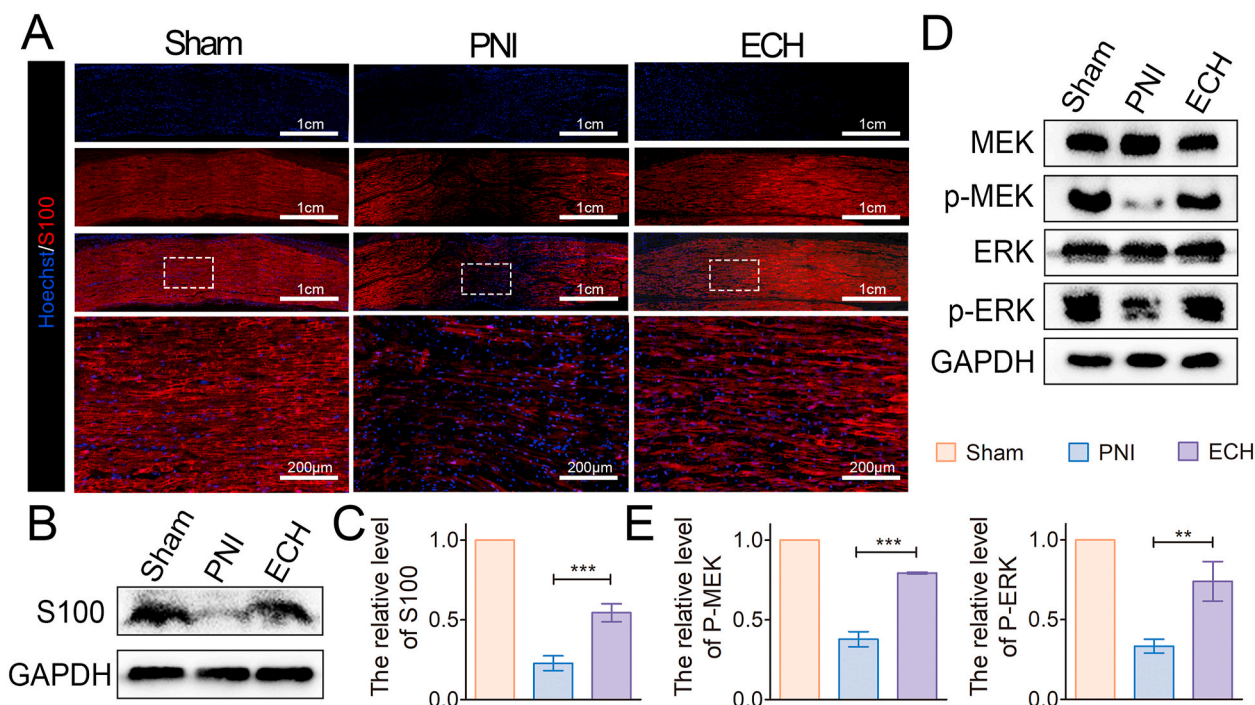


Fig. 6. Axonal remyelination of the regenerated axons after ECH treatment. (A) Immunocytochemistry of the S-100β (red) proteins in the regenerated tissues on the 28th day after the injury. (B) Expression levels of the S-100β protein in each group. (C) Quantitative analysis of western blot (n = 3) (D) Expression levels of the MEK/ERK pathway proteins. (E–F) Quantitative analysis of the protein expression, normalized to the sham group (n = 3). (*p < 0.05, **p < 0.01, and ***p < 0.001). (For interpretation of the references to color in this figure legend, the reader is referred to the Web version of this article.)

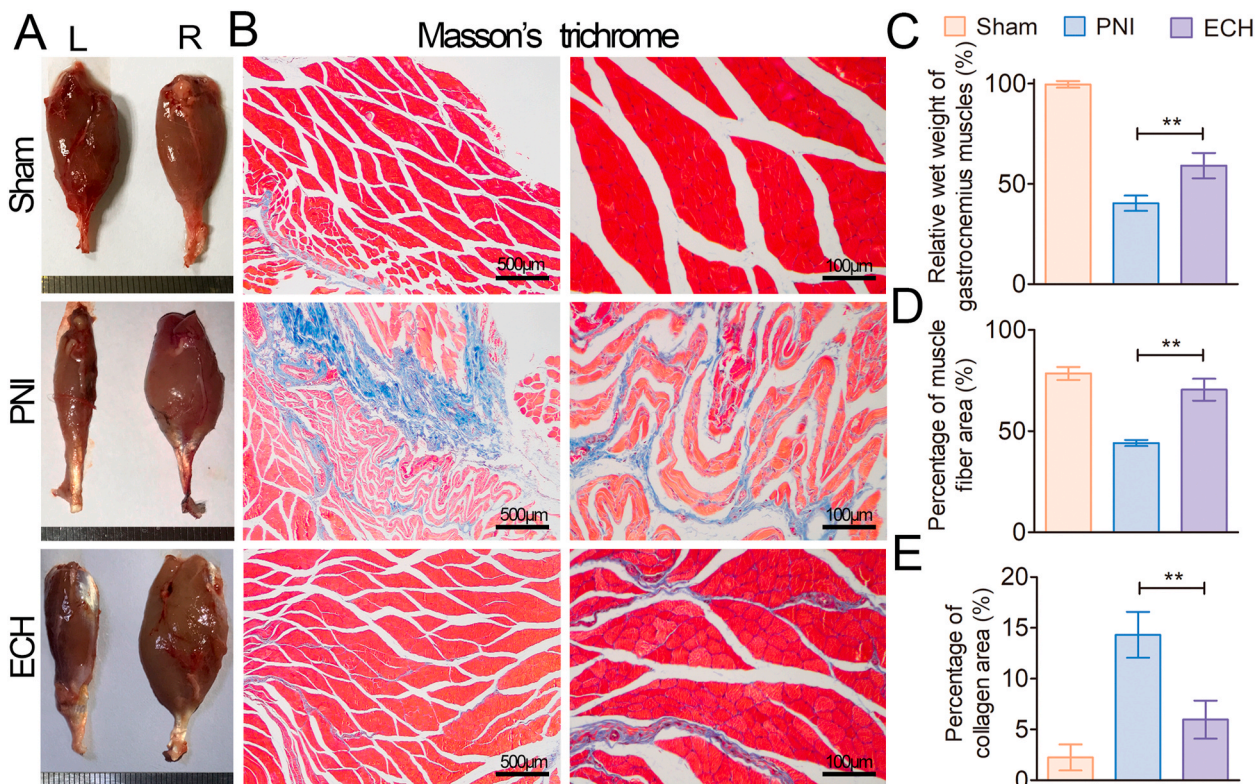


Fig. 7. Attenuation of gastrocnemius muscle atrophy after ECH treatment. (A) Gross images of the isolated gastrocnemius muscles in each group. (B) The cross-sectional view of the ipsilateral muscles highlighted by Masson's trichrome stain. (C–E) Statistical analysis of the (C) wet weight ratio of the gastrocnemius muscle, (D) percentage of muscle fiber, and (E) percentage of collagen deposits area (n = 3) (*p < 0.05, **p < 0.01, and ***p < 0.001).

with electrogenic neural tissues, thereby promoting axon regeneration and myelination.

The MEK/ERK signaling pathway is crucial for the regulation of the endogenous growth function and is closely related to the survival, proliferation, and development of nerve cells [41,42]. The activation of these distinct pathways is related to electrical participation. The underlying mechanisms of axon regeneration and remyelination were studied by evaluating the relative protein expressions of p-MEK, MEK, p-ERK, and ERK by WB. The expression levels of p-MEK and p-ERK in the ECH group were significantly higher than those in the PNI group. However, the total amount of these proteins was identical in both growth conditions (Fig. 6D and E). This indicates that the ECH facilitated axon extension and remyelination by activating the MEK/ERK signaling pathways.

3.7. Attenuation of gastrocnemius muscle atrophy by ECH treatment

Gastrocnemius muscle atrophy can serve as an indicator of functional regeneration after a sciatic nerve injury [15]. Gross views of the gastrocnemius muscle revealed that the muscle of the injured side significantly atrophied in comparison to that of the contralateral side, especially in the PNI group (Fig. 7A). A histological examination was performed using MTS to conduct a gross observation of the target gastrocnemius muscle. Evident signs of atrophy, such as disordered muscle fibers and the existence of hyperplastic collagen fibers around them, were observed in the PNI group. However, these signs were significantly attenuated by the improved nerve reinnervation in the ECH

group, which demonstrated larger muscle fibers and smaller collagen deposits than the other groups (Fig. 7B). Greater muscle weight and fiber density further confirmed that the implantation of the ECH in the PNI model facilitated the recovery of muscle fibers (Fig. 7C and D). The percentage of collagen fiber area in the ECH group ($5.9 \pm 1.9\%$) was lower than that in the PNI group ($14.3 \pm 2.7\%$) (Fig. 7E). These results indicated that the ECH treatment restored muscle function and morphology, in addition to reducing atrophy.

3.8. TEM and morphological analyses

TEM and TBS were used to assess the remyelination of the cross-sections of the regenerated sciatic nerve. The morphology and parameters of the nerve fibers, such as the myelinated axon diameters, myelinated axon density, myelin sheath thickness, and G-ratio, were further quantitative analyzed. The TBS images indicated that the regenerated nerve had myelinated to a greater extent in the ECH group than it had in the injured group, wherein the myelin sheath structure was disordered and almost invisible (Fig. 8A). The TEM morphology of the diabetic rats displayed thick electron-dense but vacuole-like defects in the myelin sheaths, which could be a consequence of the demyelination caused by diabetes. However, the regenerated axons in the ECH treated models were surrounded by clear, thick, and electron-dense myelin sheaths in comparison to those of the PNI group whose sciatic nerve remained messy, thin, and loose (Fig. 8B). The diameter and density of the remyelinated axons in the ECH group were larger than those in the PNI group (Fig. 8C and D). A statistical analysis of the

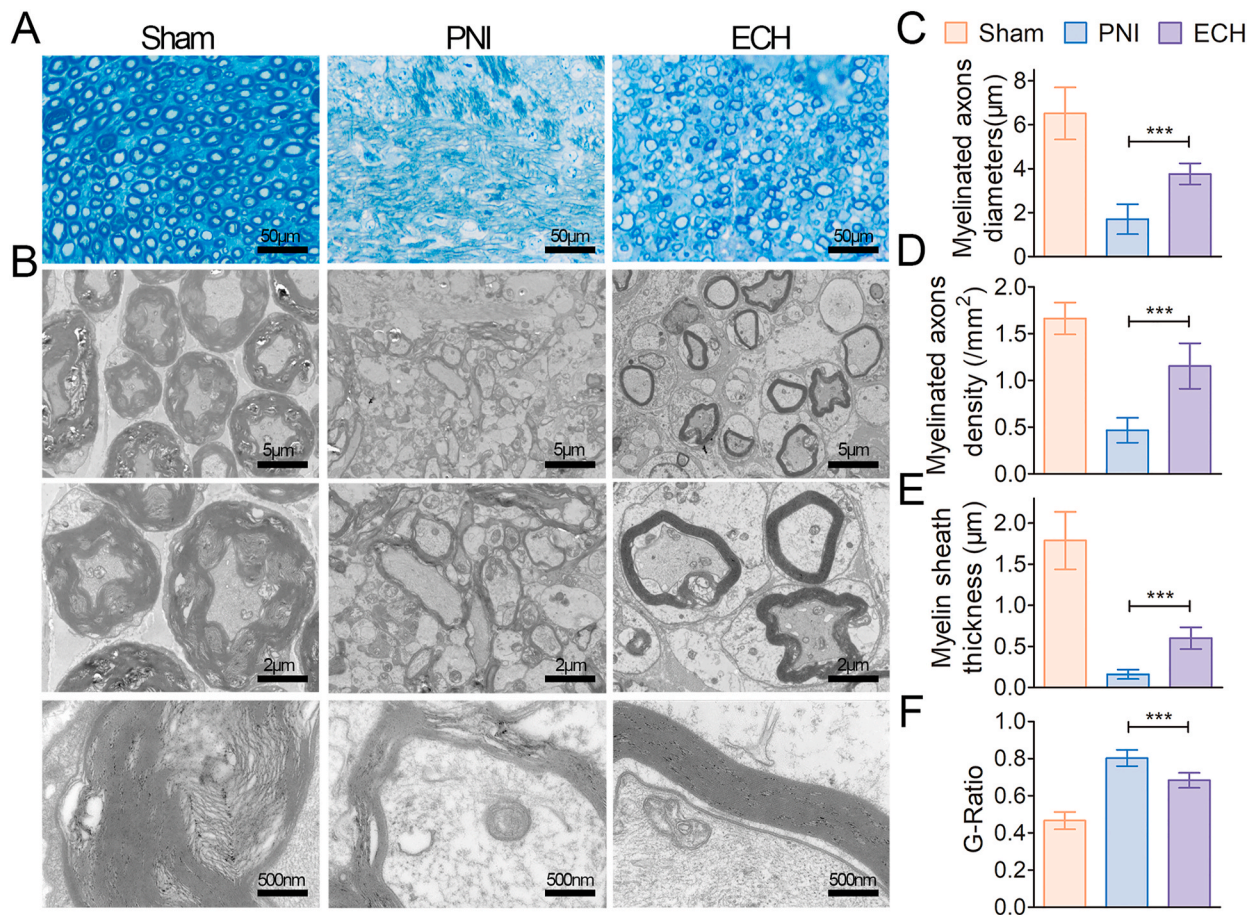


Fig. 8. Morphological evaluation of the myelination of the regenerated axons. (A) Toluidine blue staining indicating remyelination of the regenerated nerve (B) Representative TEM images of the regenerated sciatic nerve. (C–F) Histogram analysis of the remyelination of the regenerated axons through four parameters, namely (C) myelinated axon diameter, (D) myelinated axon density, (E) myelin sheath thickness, and (F) G-Ratio ($n = 3$) (* $p < 0.05$, ** $p < 0.01$, and *** $p < 0.001$). (For interpretation of the references to color in this figure legend, the reader is referred to the Web version of this article.)

myelin sheath proved that its thickness in the ECH group ($0.60 \pm 0.13 \mu\text{m}$) was greater than that in the PNI group ($0.16 \pm 0.06 \mu\text{m}$) (Fig. 8E). The G-ratio, equal to the ratio of inner axonal diameter to the total outer fiber diameter, is related to the speed of conduction, and therefore reflects axonal function and integrity. The G-ratios of normal sciatic nerves in young rats were 0.60 ± 0.04 [43]. The G-ratio of the ECH treatment (0.68 ± 0.04) was smaller than that of the PNI group (0.80 ± 0.04), which is consistent with the TEM results (Fig. 8F). The smaller G-ratio indicated better remyelination of the regenerated nerves. These results suggested that the demyelinated nerve in diabetic PNI model rats can be better repaired through ECH treatment.

4. Conclusion

We developed biocompatible ECHs with porous, highly conductive, soft, and adhesive properties in this study. These properties of the ECHs, which were developed by mixing TA, Py, and Fe^{3+} , were identical to those of a surgical or wound dressing. The thin film-like hydrogel dressing can be easily attached to the nerve fibers and automatically forms a tubular structure, which simplifies the cumbersome installation process during the treatment of PNI in DM patients. These properties of the ECH facilitated SC attachment and migration in addition to promoting axonal extension *in vitro*. The *in vivo* experiments proved that ECHs could stimulate axonal regeneration and remyelination in DM rats. Further, the hydrogel facilitated nerve impulse transmission and muscle receptivity, thereby preventing muscle denervation atrophy and promoting functional recovery. The ECH dressing is a promising candidate for improving nerve regeneration and promoting muscle function recovery in diabetic nerve injury.

CRedit authorship contribution statement

Can Liu: Conceptualization, Methodology, Formal analysis, Writing – original draft. **Lei Fan:** Conceptualization, Methodology, Investigation, Data curation. **Zhenming Tian:** Methodology, Validation, Writing – original draft. **Huiquan Wen:** Methodology, Investigation. **Lei Zhou:** Methodology, Investigation, Resources. **Pengfei Guan:** Methodology, Data curation. **Yian Luo:** Methodology, Formal analysis. **Chuncheung Chan:** Methodology, Data curation. **Guoxin Tan:** Investigation. **Chengyun Ning:** Conceptualization, Validation, Supervision. **Limin Rong:** Conceptualization, Resources, Supervision. **Bin Liu:** Conceptualization, Formal analysis, Supervision.

Declaration of competing interest

The authors declare that they have no known competing financial interests or personal relationships that could have appeared to influence the work reported in this paper.

Acknowledgements

We thank Lei Fan for his help in drawing the schematic diagram and typesetting figures. This study was supported by the National Key Research and Development Program of China (2017YFA0105400); the National Natural Science Foundation of China (82072455, 81772349, 31470949); the Guangdong Basic and Applied Basic Research Foundation (2019A1515012181, 2017A030313594) and the Guangzhou Science and Technology Planning Project of China (201707010115).

Appendix A. Supplementary data

Supplementary data related to this article can be found at <https://doi.org/10.1016/j.bioactmat.2021.03.034>.

References

- [1] D.R. Whiting, L. Guariguata, C. Weil, J. Shaw, IDF diabetes atlas: global estimates of the prevalence of diabetes for 2011 and 2030, *Diabetes Res. Clin. Pract.* 94 (3) (2011) 311–321.
- [2] E.L. Feldman, K.-A. Nave, T.S. Jensen, D.L.H. Bennett, New horizons in diabetic neuropathy: mechanisms, bioenergetics, and pain, *Neuron* 93 (6) (2017) 1296–1313.
- [3] B.C. Callaghan, H.T. Cheng, C.L. Stables, A.L. Smith, E.L. Feldman, Diabetic neuropathy: clinical manifestations and current treatments, *Lancet Neurol.* 11 (6) (2012) 521–534.
- [4] J. Zenker, D. Ziegler, R. Chrast, Novel pathogenic pathways in diabetic neuropathy, *Trends Neurosci.* 36 (8) (2013) 439–449.
- [5] R. Li, Y. Li, Y. Wu, Y. Zhao, H. Chen, Y. Yuan, K. Xu, H. Zhang, Y. Lu, J. Wang, X. Li, X. Jia, J. Xiao, Heparin-poloxamer thermosensitive hydrogel loaded with bFGF and NGF enhances peripheral nerve regeneration in diabetic rats, *Biomaterials* 168 (2018) 24–37.
- [6] L. Conforti, J. Gilley, M.P. Coleman, Wallerian degeneration: an emerging axon death pathway linking injury and disease, *Nat. Rev. Neurosci.* 15 (6) (2014) 394–409.
- [7] L. Zhou, L. Fan, X. Yi, Z. Zhou, C. Liu, R. Fu, C. Dai, Z. Wang, X. Chen, P. Yu, D. Chen, G. Tan, Q. Wang, C. Ning, Soft conducting polymer hydrogels cross-linked and doped by tannic acid for spinal cord injury repair, *ACS Nano* 12 (11) (2018) 10957–10967.
- [8] J. Moskow, B. Ferrigno, N. Mistry, D. Jaiswal, K. Bulsara, S. Rudraiah, S. G. Kumbhar, Review: bioengineering approach for the repair and regeneration of peripheral nerve, *Bioact. Mater.* 4 (1) (2019) 107–113.
- [9] Y. Liu, J. Liu, S. Chen, T. Lei, Y. Kim, S. Niu, H. Wang, X. Wang, A.M. Foudeh, J. B. Tok, Z. Bao, Soft and elastic hydrogel-based microelectronics for localized low-voltage neuromodulation, *Nat. Biomed. Eng.* 3 (1) (2019) 58–68.
- [10] Y. Qian, Y. Cheng, J. Song, Y. Xu, W.E. Yuan, C. Fan, X. Zheng, Mechano-informed biomimetic polymer scaffolds by incorporating self-powered zinc oxide nanogenerators enhance motor recovery and neural function, *Small* 16 (32) (2020) 2000796.
- [11] R. Balint, N.J. Cassidy, S.H. Cartmell, Conductive polymers: towards a smart biomaterial for tissue engineering, *Acta Biomater.* 10 (6) (2014) 2341–2353.
- [12] Y. Qian, X. Zhao, Q. Han, W. Chen, H. Li, W. Yuan, An integrated multi-layer 3D-fabrication of PDA/RGD coated graphene loaded PCL nanoscaffold for peripheral nerve restoration, *Nat. Commun.* 9 (1) (2018).
- [13] S.P. Lacour, G. Courtine, J. Guck, Materials and technologies for soft implantable neuroprostheses, *Nat. Rev. Mater.* 1 (10) (2016).
- [14] D. Xu, L. Fan, L. Gao, Y. Xiong, Y. Wang, Q. Ye, A. Yu, H. Dai, Y. Yin, J. Cai, L. Zhang, Micro-nanostructured polyaniline assembled in cellulose matrix via interfacial polymerization for applications in nerve regeneration, *ACS Appl. Mater. Interfaces* 8 (27) (2016) 17090–17097.
- [15] Y.S. Choi, Y.-Y. Hsueh, J. Koo, Q. Yang, R. Avila, B. Hu, Z. Xie, G. Lee, Z. Ning, C. Liu, Y. Xu, Y.J. Lee, W. Zhao, J. Fang, Y. Deng, S.M. Lee, A. Vázquez-Guardado, I. Stepien, Y. Yan, J.W. Song, C. Haney, Y.S. Oh, W. Liu, H.-J. Yoon, A. Banks, M. R. MacEwan, G.A. Ameer, W.Z. Ray, Y. Huang, T. Xie, C.K. Franz, S. Li, J.A. Rogers, Stretchable, dynamic covalent polymers for soft, long-lived bioresorbable electronic stimulators designed to facilitate neuromuscular regeneration, *Nat. Commun.* 11 (1) (2020).
- [16] A. Lemke, J. Ferguson, K. Gross, C. Penzenstadler, M. Bradl, R.L. Mayer, C. Gerner, H. Redl, S. Wolbank, Transplantation of human amnion prevents recurring adhesions and ameliorates fibrosis in a rat model of sciatic nerve scarring, *Acta Biomater.* 66 (2018) 335–349.
- [17] J. Isaacs, S. Mallu, W. Yan, B. Little, Consequences of oversizing: nerve-to-nerve tube diameter mismatch, *J. Bone Joint Surg. Am.* 96 (17) (2014) 1461–1467.
- [18] R. Urie, D. Ghosh, I. Ridha, K. Rege, Inorganic nanomaterials for soft tissue repair and regeneration, *Annu. Rev. Biomed. Eng.* 20 (1) (2018) 353–374.
- [19] X. Zhao, H. Wu, B. Guo, R. Dong, Y. Qiu, P.X. Ma, Antibacterial anti-oxidant electroactive injectable hydrogel as self-healing wound dressing with hemostasis and adhesiveness for cutaneous wound healing, *Biomaterials* 122 (2017) 34–47.
- [20] D.L. Taylor, M. in het Panhuis, Self-healing hydrogels, *Adv. Mater.* 28 (41) (2016) 9060–9093.
- [21] J. Tao, Y. Hu, S. Wang, J. Zhang, X. Liu, Z. Gou, H. Cheng, Q. Liu, Q. Zhang, S. You, M. Gou, A 3D-engineered porous conduit for peripheral nerve repair, *Sci. Rep.* 7 (2017) 46038.
- [22] J. Zhang, Y. Chen, Y. Huang, W. Wu, X. Deng, H. Liu, R. Li, J. Tao, X. Li, X. Liu, M. Gou, A 3D-printed self-adhesive bandage with drug release for peripheral nerve repair, *Adv. Sci.* 7 (23) (2020) 2002601.
- [23] M.A. Lopez-Verrilli, F. Picou, F.A. Court, Schwann cell-derived exosomes enhance axonal regeneration in the peripheral nervous system, *Glia* 61 (11) (2013) 1795–1806.
- [24] J.S.G. Lawrence, J. Coppey, Eric P. Davidson, Joyce A. Dunlap, Donald D. Lund, Mark A. Yorek, Effect of antioxidant treatment of streptozotocin-induced diabetic rats on endoneurial blood flow, motor nerve conduction velocity, and vascular reactivity of epineurial arterioles of the sciatic nerve, *Diabetes* 50(8) (2001) 1927–1937.
- [25] T.L. Lopez-Silva, C.D. Cristobal, C.S. Edwin Lai, V. Leyva-Aranda, H.K. Lee, J. D. Hartgerink, Self-assembling multidomain peptide hydrogels accelerate peripheral nerve regeneration after crush injury, *Biomaterials* 265 (2021) 120401.
- [26] V. Bucan, D. Vaslaitis, C.-T. Peck, S. Strauß, P.M. Vogt, C. Radtke, Effect of exosomes from rat adipose-derived mesenchymal stem cells on neurite outgrowth and sciatic nerve regeneration after crush injury, *Mol. Neurobiol.* 56 (3) (2018) 1812–1824.

- [27] T. Lin, S. Liu, S. Chen, S. Qiu, Z. Rao, J. Liu, S. Zhu, L. Yan, H. Mao, Q. Zhu, D. Quan, X. Liu, Hydrogel derived from porcine decellularized nerve tissue as a promising biomaterial for repairing peripheral nerve defects, *Acta Biomater.* 73 (2018) 326–338.
- [28] L. Zhou, G. Tan, K. Ouyang, Y. Liu, C. Ning, Highly water-dispersible, highly conductive, and biocompatible polypyrrole-coated silica particles stabilized and doped by chondroitin sulfate, *Part. Part. Syst. Char.* 32 (12) (2015) 1068–1077.
- [29] D.R. Griffin, W.M. Weaver, P.O. Scumpia, D. Di Carlo, T. Segura, Accelerated wound healing by injectable microporous gel scaffolds assembled from annealed building blocks, *Nat. Mater.* 14 (7) (2015) 737–744.
- [30] J. Wang, H. Xiong, T. Zhu, Y. Liu, H. Pan, C. Fan, X. Zhao, W.W. Lu, Bioinspired multichannel nerve guidance conduit based on shape memory nanofibers for potential application in peripheral nerve repair, *ACS Nano* 14 (10) (2020) 12579–12595.
- [31] R.A. Green, N.H. Lovell, G.G. Wallace, L.A. Poole-Warren, Conducting polymers for neural interfaces: challenges in developing an effective long-term implant, *Biomaterials* 29 (24–25) (2008) 3393–3399.
- [32] C. Ning, L. Zhou, G. Tan, Fourth-generation biomedical materials, *Mater. Today* 19 (1) (2016) 2–3.
- [33] L. He, Q. Xiao, Y. Zhao, J. Li, S. Reddy, X. Shi, X. Su, K. Chiu, S. Ramakrishna, Engineering an injectable electroactive nanohybrid hydrogel for boosting peripheral nerve growth and myelination in combination with electrical stimulation, *ACS Appl. Mater. Interfaces* 12 (47) (2020) 53150–53163.
- [34] K.H. Vining, D.J. Mooney, Mechanical forces direct stem cell behaviour in development and regeneration, *Nat. Rev. Mol. Cell Biol.* 18 (12) (2017) 728–742.
- [35] C. Liu, L. Fan, J. Xing, Q. Wang, C. Lin, C. Liu, X. Deng, C. Ning, L. Zhou, L. Rong, B. Liu, Inhibition of astrocytic differentiation of transplanted neural stem cells by chondroitin sulfate methacrylate hydrogels for the repair of injured spinal cord, *Biomater. Sci.* 7 (5) (2019) 1995–2008.
- [36] N.P. Goncalves, C.B. Vaegter, H. Andersen, L. Ostergaard, N.A. Calcutt, T.S. Jensen, Schwann cell interactions with axons and microvessels in diabetic neuropathy, *Nat. Rev. Neurol.* 13 (3) (2017) 135–147.
- [37] A. Bozkurt, R. Deumens, J. Scheffel, D.M. O'Dey, J. Weis, E.A. Joosten, T. Führmann, G.A. Brook, N. Pallua, CatWalk gait analysis in assessment of functional recovery after sciatic nerve injury, *J. Neurosci. Methods* 173 (1) (2008) 91–98.
- [38] J. Du, J. Liu, S. Yao, H. Mao, J. Peng, X. Sun, Z. Cao, Y. Yang, B. Xiao, Y. Wang, P. Tang, X. Wang, Prompt peripheral nerve regeneration induced by a hierarchically aligned fibrin nanofiber hydrogel, *Acta Biomater.* 55 (2017) 296–309.
- [39] N.C. Spitzer, Electrical activity in early neuronal development, *Nature* 444 (7120) (2006) 707–712.
- [40] A.G. Blankenship, M.B. Feller, Mechanisms underlying spontaneous patterned activity in developing neural circuits, *Nat. Rev. Neurosci.* 11 (1) (2010) 18–29.
- [41] I. Napoli, L.A. Noon, S. Ribeiro, A.P. Kerai, S. Parrinello, L.H. Rosenberg, M. J. Collins, M.C. Harrisingh, I.J. White, A. Woodhoo, A.C. Lloyd, A central role for the ERK-signaling pathway in controlling Schwann cell plasticity and peripheral nerve regeneration in vivo, *Neuron* 73 (4) (2012) 729–742.
- [42] T.D. Glenn, W.S. Talbot, Signals regulating myelination in peripheral nerves and the Schwann cell response to injury, *Curr. Opin. Neurobiol.* 23 (6) (2013) 1041–1048.
- [43] M.B. Christensen, P.A. Tresco, Differences exist in the left and right sciatic nerves of naive rats and cats, *Anat. Rec.* 298 (8) (2015) 1492–1501.